Enhanced bone regeneration via endochondral ossification using Exendin-4-modified mesenchymal stem cells

Zihao He [a,b,1], Hui Li [a,b,1], Yuanyuan Zhang [c], Shuang Gao [c], Kaini Liang [c], Yiqi Su [a,b], Yanan Du [c,*], Du Wang [a,b], Dan Xing [a,b,**], Zhen Yang [a,b], Jianhao Lin [a,b,***]

[a] *Arthritis Clinic & Research Center, Peking University People's Hospital, Peking University, Beijing, 100044, China*
[b] *Arthritis Institute, Peking University, Beijing, 100044, China*
[c] *Department of Biomedical Engineering, School of Medicine, Tsinghua-Peking Center for Life Sciences, MOE Key Laboratory of Bioorganic Phosphorus Chemistry and Chemical Biology, Tsinghua University, Beijing, 100084, China*

ARTICLE INFO

ABSTRACT

Nonunions and delayed unions pose significant challenges in orthopedic treatment, with current therapies often proving inadequate. Bone tissue engineering (BTE), particularly through endochondral ossification (ECO), emerges as a promising strategy for addressing critical bone defects. This study introduces mesenchymal stem cells overexpressing Exendin-4 (MSC-E4), designed to modulate bone remodeling via their autocrine and paracrine functions. We established a type I collagen (Col-I) sponge-based *in vitro* model that effectively recapitulates the ECO pathway. MSC-E4 demonstrated superior chondrogenic and hypertrophic differentiation and enhanced the ECO cell fate in single-cell sequencing analysis. Furthermore, MSC-E4 encapsulated in microscaffold, effectively facilitated bone regeneration in a rat calvarial defect model, underscoring its potential as a therapeutic agent for bone regeneration. Our findings advocate for MSC-E4 within a BTE framework as a novel and potent approach for treating significant bone defects, leveraging the intrinsic ECO process.

1. Introduction

Nonunions and delayed unions not only represent significant clinical challenges but also pose substantial implications for patients' quality of life and healthcare systems. Accounting for approximately 10 % of all fractures [1], they are often linked to prolonged hospital stays, increased medical expenses, and long-term functional and psychological consequences. Each year, an estimated 100,000 fractures in the United States progress to nonunion, highlighting the vast number of individuals grappling with its repercussions [2]. These conditions, characterized by pain, functional impairment, and significant psychological distress [3], demand efficient therapeutic interventions. A prevalent causative factor is critical-size defects—defined as the smallest intraosseous wound that

will not spontaneously heal, emphasizing the gravity of such defects in bone repair processes [4]. Despite the availability of various treatments, many conventional methods, especially operative fixations, often overlook the intricate biological aspects of bone healing, leading to suboptimal outcomes and recurrent medical consultations [5]. Recognizing these challenges, the scientific community is increasingly veering towards bone tissue engineering (BTE) as a promising avenue [6].

BTE, an avant-garde interdisciplinary domain, integrates principles of bioengineering, cellular transplantation, and materials science to devise biological alternatives that can effectively mend injured bone [7]. This approach harnesses the synergy of stem cells, scaffolds, and growth factors to recreate an optimal biomimetic milieu that fosters the regeneration of native tissues and cells [8]. Mesenchymal stem cells

(MSCs), owing to their multilineage differentiation potential and innate ability to target and repair tissue damage, emerge as promising candidates for bone regeneration [9]. Notably, MSC-derived secreted bioactive molecules can modulate the immune response, amplifying tissue regenerative capabilities [10]. Genetic engineering offers a method to further potentiate MSCs' therapeutic benefits, enabling the production of specific trophic cytokines or other advantageous gene products in experimental models [11,12].

Three-dimensional (3D) *in vitro* models surpass traditional 2D cellular counterparts by more closely emulating the *in vivo* cellular milieu characterized by multi-dimensional cell-cell interactions [13]. Microscaffolds employed in 3D micro-tissue culture systems aim to foster cellular interactions and potentiate extracellular matrix (ECM) secretion [10]. Prior investigations conducted by our team underscored the significance of microscaffold encapsulation, highlighting its role in providing an essential 3D microenvironment conducive to tissue repair [14]. Furthermore, we delved into the application of 3D microscaffolds infused with MSCs in addressing rat calvarial defects [15,16]. Such endeavors corroborated the practicality of the proposed *in vivo* system for cell therapy and in-depth mechanistic scrutiny. Consequently, the amalgamation of *in vitro* engineering models with 3D microscaffold systems emerges as a promising avenue for bone regeneration.

Endochondral ossification (ECO) stands as a paramount pathway underpinning bone morphogenesis and rejuvenation, commencing with cartilaginous mold establishment [17]. This intricate process sees the aggregation of MSCs differentiating into nascent chondrocytes, which in turn synthesize glycosaminoglycan and cartilage-specific matrix proteins. The ensuing maturation stages witness chondrocyte proliferation, with their terminal differentiation hallmarked by hypertrophy, type X collagen (Col-X) expression, and matrix calcification. ECO's distinct capability to persevere in hypoxic conditions and foster neovascularization alongside ossification is noteworthy [18]. By mimicking the local niche, MSCs implicated in the ECO cascade offer an insightful avenue to explore *in vitro* bone remodeling. Developmental engineering constructs thus emerge as bio-inspired templates, accelerating bone revival in extensive defect sites [19,20]. Contemporary research centered on ECO's role in calvarial defect repair has unearthed the contributions of skeletal stem cells residing in calvarial sutures to post-fracture ECO, despite the calvaria being primarily associated with intramembranous ossification [21,22]. Hence, devising an *in vitro* engineering paradigm that adeptly replicates ECO regulatory dynamics remains indispensable for bone regeneration research.

Incretins, encompassing glucose-dependent insulinotropic polypeptide (GIP) and glucagon-like peptide 1 (GLP-1), purportedly influence bone homeostasis within the gut-bone axis [23]. The GLP-1 receptor (GLP-1R), categorized as a class B G protein-coupled receptor, exhibits crucial roles in bone dynamics. Demonstratively, GLP-1R deficient mice (Glp-1r−/−) manifest reduced cortical bone mass in spinal and tibial regions [24], concurrently revealing compromised biomechanical attributes and maturation of the collagen matrix [25]. Intriguingly, GLP-1R presence in bone constituents suggests GLP-1R agonists (GLP-1RAs) as influential agents in bone remodeling, notably during regenerative phases [24,26]. Certain GLP-1RAs, including exenatide (exendin-4) [27–31] and liraglutide [32–35], have been validated to foster bone genesis in varied pathological models, such as post-ovariectomy, type 2 diabetes, and hyperlipidemia. Complementary findings associate exendin-4 with a diminished bone fracture propensity [36]. Nonetheless, constraints tied to localized delivery and fleeting half-life circumscribe the therapeutic potential of GLP-RAs, exendin-4 included, in bone rejuvenation. In preceding investigations, we engineered MSCs fortified with exendin-4 (MSC-E4) and discerned their sustained therapeutic efficacy in diabetes mitigation, amplified by autocrine and paracrine synergies with our documented 3D microscaffold [37]. The aim of this study is to evaluate the efficacy of MSC-E4 in fostering endochondral ossification for augmented bone regeneration. In this discourse, we elucidate the propensity of MSC-E4 to augment ECO via autocrine and paracrine modalities. A pioneering *in vitro* ECO prototype was also introduced, simulating genuine ECO dynamics, wherein distinct cellular subsets and developmental trajectories were demystified through single-cell sequencing. The culmination of our endeavor realized bone regeneration by harmonizing MSC-E4 with microscaffolds in *vivo* contexts.

2. Results

2.1. Study design

Fig. 1 encapsulates the overarching schema of our investigation. Commencing with the bioengineering of MSC-E4 via lentiviral transduction, we delved into its potential in modulating bone turnover, elucidating both its autocrine and paracrine influences on osteogenesis and osteoclastogenesis. The unique attributes of MSC-E4 were further probed, particularly its competency to facilitate *in vitro* ECO within a type I collagen (Col-I) matrix. Transcending *in vitro* assessments, an amalgamation of MSC-E4 and microscaffold encapsulation was harnessed for bone regenerative applications, specifically within a rat critical-sized calvarial defect paradigm.

### 2.2. Construction of MSC-E4 and its anti-aging and anti-apoptosis activity

We have successfully constructed the MSC-E4 derived from human umbilical cord MSCs using a lentivirus-mediated transfection approach (Fig. 2A). Examination under light microscopy demonstrated no noticeable morphological distinctions between MSC-E4 and MSC-C (Fig. 2B). The MSC-E4 cells preserved the typical MSC surface marker expression (Fig. S1 A). Additionally, both cell types maintained similar viability profiles (Fig. S1B).

Remarkably, Exendin-4 expression in MSC-E4 manifested a surge, with levels amplifying by approximately 10,000-fold at the mRNA level as gauged by qRT-PCR (Fig. 2C). ELISA assessments of the extracellular medium showed a 20-fold increase in Exendin-4 protein levels (Fig. 2D), and this finding was corroborated by Western blot analysis (Fig. 2E). In contrast, only trace amounts of Exendin-4 were discerned in exosomes (Fig. S1 C & D) relative to the conditioned medium (CM) post-ultrafiltration, implying that Exendin-4 is not predominantly secreted via exosomes. This secretion pattern is consistent with our previous observations [37]. Consequently, we believe that CM obtained through ultrafiltration adequately represents the complete secretome, encompassing exosomes, for the functional examination of MSC-E4.

Functionally, MSC-E4 presented a heightened resilience against ROS. In the presence of H2O2-induced oxidative stress, MSC-E4 also showcased marked anti-apoptotic and anti-aging capabilities (Fig. 2F–H), which are in agreement with previously reported research [37].

2.3. Enrichment analysis of MSC-E4 by secretome and transcriptome

We employed an ultrafiltration technique to isolate the secretome from MSC-C and MSC-E4, followed by detailed liquid chromatography-mass spectrometry (LC-MS) analysis (Fig. 3 A-C, S2 A-B). The secretome analysis identify differential expression in 146 proteins, with 39 exhibiting pronounced secretion discrepancies (Fig. 3 B). A subset of these genes were intricately associated with the extracellular matrix, collagen binding and cell communication in GO (Fig. S2 A) and KEGG (Fig. S2 B) enrichment analysis. Protein-Protein Interaction (PPI) network analysis demonstrated that these proteins predominantly associate with cellular components and are central to the metabolism and organization of the extracellular matrix (Fig. 3C). Transcriptome profiling clearly differentiated the global gene expression profiles of MSC-E4 from MSC-C (Fig. 3D), identifying 898 differentially expressed genes (DEGs) between the two groups (Fig. 3E and F). GO enrichment analysis highlighted alterations related to the ECM and cytoskeleton (Fig. S2C). KEGG enrichment underscored the pivotal role of multiple
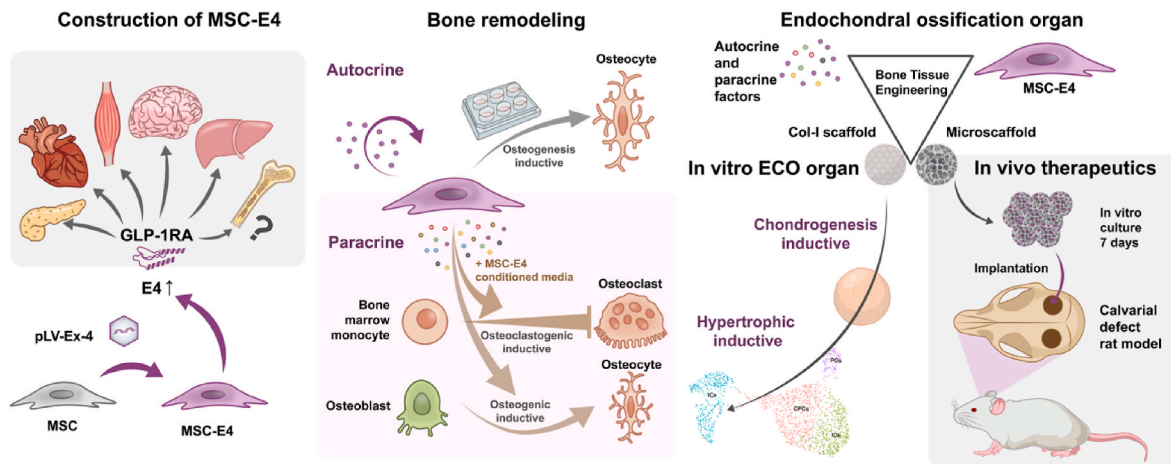
Fig. 1. Conceptual overview of the investigative framework. The left segment delineates the bioengineering of MSC-E4. Central segment elucidate autocrine and paracrine-mediated bone remodeling dynamics. The final segment of our study confirms that MSC-E4, encapsulated within a collagen sponge or a microscaffold, effectively enhances bone regeneration through the ECO process, as demonstrated in both *in vitro* and *in vivo* models, aligning with the principles of BTE.

pathways, including Wnt and PI3K-Akt, in bone remodeling (Fig. 3 G & H). Integrating the findings from secretomic and transcriptomic analyses, we propose that MSC-E4 may play a functional role in bone remodeling through both autocrine and paracrine mechanisms.

2.4. MSC-E4 modulates bone remodeling through autocrine and paracrine mechanisms

To discern the role of MSC-E4 in bone remodeling, we initially focused on its autocrine effects on osteogenic differentiation (Fig. 4 A). During osteogenic induction, MSC-E4 exhibited notable ALP activity by day 7 (Fig. 4 B), and by day 21, there was significant mineralization (Fig. 4C & D). Essential osteogenic markers, such as ALP, COL1A1, and RUNX2, were upregulated by day 7 (Fig. 4 E). Notably, Exendin-4 levels in the CM remained stable throughout the osteogenic induction period (Fig. 4 F).

Regarding paracrine effects, we assessed the influence of MSC-E4 CM on the osteogenic differentiation of MLO-A5 cells, a late osteoblast-early osteocyte lineage, and on osteoclast differentiation of mouse bone marrow macrophages (BMMs) (Fig. 4 G). When MLO-A5 cells were treated with CM along with osteogenic induction solution, enhanced ALP staining was evident at day 7 (Fig. 4H), with marked increases in mineralization by day 14 (Fig. 4 I & J). Additionally, there was a significant upregulation in mRNA expression of osteogenic markers Runx2 and Ocn.

In mouse BMM osteoclastogenesis, we observed a noticeable reduction in Trap-positive osteoclasts (Fig. 4 L), with quantitative analysis revealing a significant decrease in both the size and number of Trap-positive cells (Fig. 4 M). MSC-E4 CM induced a reduction in osteoclastogenic gene markers, including Trap, Ctsk, and Dcstamp (Fig. 4 N).

2.5. MSC-E4 mediated endochondral osteogenesis: an in vitro model

In the MSC-E4 sequencing results, a potential for ECM regulation was unveiled, which, when compared with a previously compiled list of 33 cartilage-specific proteins [38,39] (Fig. S3A), revealed a set of 15 common proteins (Fig. S3 B). Given both the autocrine and paracrine roles of MSC-E4 in bone remodeling, delving into mechanisms within the context of ECO is of significant value. The ECO pathway involves the differentiation of MSCs through chondrogenesis, which accelerates fibrosis and ECM mineralization via hypertrophic chondrocyte formation, culminating in osteogenesis. To simulate this process, an *in vitro* ECO model was developed. Leveraging the facilitative properties of Col-I ECM on MSC condensation [40] and its role in stimulating cell

proliferation and differentiation within limb-bud mesenchyme cell cultures [41], our design drew inspiration from established models [42–44]. MSCs were embedded in a Col-I sponge matrix and subjected to 4 weeks of chondrogenesis induction followed by 2 weeks of hypertrophic induction (Fig. 5 A, Fig. S3 C).

After 4 weeks of chondrogenesis, both MSC-C and MSC-E4 exhibited typical red Safranin-O staining and positive type II collagen (Col-II) immunolocalization. MSC-E4, notably, showed intensified staining and uniformity, suggestive of enhanced cartilaginous tissue formation (Fig. 5 B). The Bern Score was significantly higher in the MSC-E4 group [44] (Fig. 5C). Following the hypertrophic stage, there was a marked increase in collagen fiber staining and Col-X expression in MSC-E4 (Fig. 5 D). Micro-CT analysis showed a higher bone volume in the MSC-E4 group (Fig. 5 E & F). After 6 weeks, an upregulation of the hypertrophic marker COL10A1 and osteoblast marker COL1A1 was observed in MSC-E4 samples, with no change in the chondrogenic marker COL2A1 (Fig. 5 G). Interestingly, Exendin-4 protein levels remained stable at week 4 but decreased during the 6-week ECO phase in CM, possibly due to the initiation of cartilage hypertrophy [44] (Fig. 5H).

2.6. Single cell sequencing in MSC-E4 ECO in vitro model

To further explore the differentiation characteristics of MSCs during ECO, samples of cell of ECO after induction for 6 weeks were digested and processed for single-cell sequencing (Fig. 6 A). Dimensionality reduction of all cellular data was visualized using UMAP (Fig. 6 B). Characteristic markers defined four subsets: cartilage progenitor cells (CPCs), intermediate chondrocytes (ICs), regulatory chondrocytes (RCs), and pre-osteoblasts (POs) (Fig. 6 D), with distinct cluster marker genes identified among DEGs, including CPCs (HMGB2, FGF2), ICs (COL1A1, COL1A2), RCs (TPT1, MIF), and POs (COL10A1, Runx2) (Fig. 6 E). CPCs are initiating cells in ECO. ICs were an intermediate state of chondrogenic differentiation. RCs are thought to govern MSC migration and proliferation [45], and POs are hypertrophic, osteogenic cells marked by COL10A1 and Runx2 expression [46].

Comparative analysis between MSC-C and MSC-E4 revealed an increase in the proportion of CPCs and POs, with a decrease in ICs and RCs in the MSC-E4 group (Fig. 6 F), suggesting MSC-E4's enhancement of osteogenesis.

Developmental trajectories of these cell subsets were mapped to understand their interrelations. The four clusters spanned two pseudo-time branches (Fig. 6 G), with branch 1 (cell fate 1) marked by increased COL10A and RUNX2 and decreased MIF and TPT1, while branch 2 (cell fate 2) showed the opposite trend (Fig. 6H & I). Cell fate 1, more closely
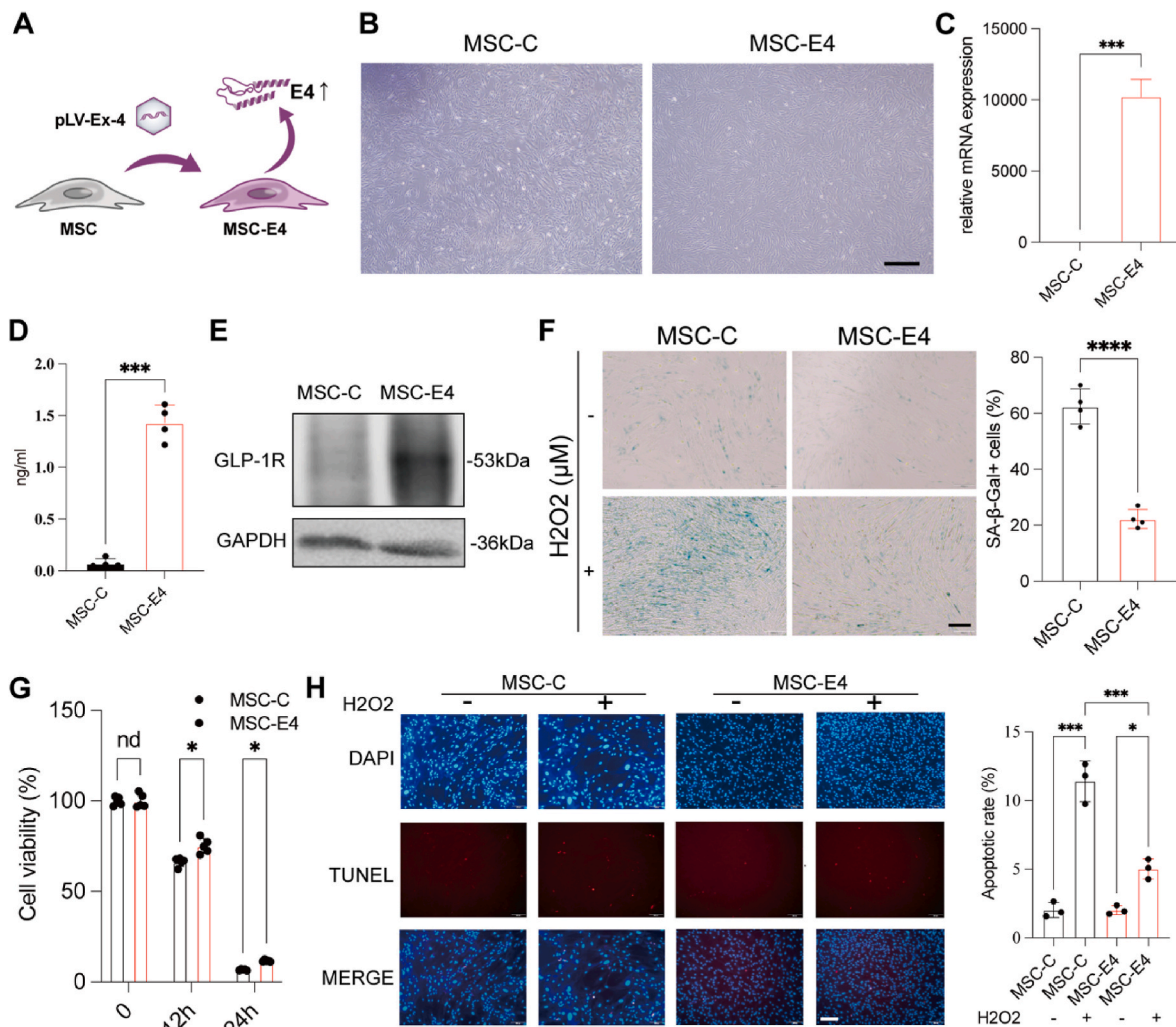
Fig. 2. Construction and Characterization of MSC-E4. A) Schematic illustration depicting the generation of MSC-E4. B) Morphological comparison of control MSCs (MSC-C) and MSC-E4 using light microscopy. C) Quantitative RT-PCR results presenting the relative mRNA expression levels of Exendin-4 in MSC-E4 as compared to MSC-C. D) Exendin-4 protein levels in the conditioned medium of MSC-E4 as determined by enzyme-linked immunosorbent assay (ELISA). E) Western blot analysis indicating the protein levels of GLP-1 receptor (GLP-1R) in MSC-C and MSC-E4. GAPDH was used as an internal loading control. F) Assessment of reactive oxygen species (ROS)-induced senescence in MSC-C and MSC-E4. The cells were stained for senescence-associated β-galactosidase (SA-β-Gal) activity in the absence (−) or presence (+) of H2O2. G) Analysis of cell viability via CCK-8 under ROS stress conditions. MSC-C and MSC-E4 were exposed to H2O2 for 0, 12, and 24 h. H) TUNEL staining of apoptosis in MSC-C and MSC-E4 after exposure to H2O2. Cells were stained with DAPI (blue) to highlight nuclei and TUNEL (red) to detect apoptotic cells. Scale bar, 200 μm. For all charts, data are presented as means ± SEM (standard error of the mean), *p < 0.05, **p < 0.01, ***p < 0.001, n ≥ 3 per group.

aligned with the ECO process (designated as ECO cell fate), saw its proportion increase within the MSC-E4 group. Conversely, cell fate 2, termed the regulatory cell fate, was reduced (Fig. S3 E).

Furthermore, KEGG and GO enrichment analyses were performed for MSC-C and MSC-E4 across different clusters (Fig. S3 F). DEGs were highlighted, implicating MSC-E4's regulatory influence on ECO (Fig. S3G).

2.7. Enhanced bone regeneration using MSC-E4 encapsulated in microscaffold in a rat critical-sized calvarial defect model

We integrated MSC-E4 with a microscaffold to assess its bone regeneration capabilities in a rat calvarial defect model (Fig. S4 A for scanning electron microscopy results). After a week of chondrogenic differentiation *in vitro*, we implanted the microscaffold into the rats 5-mm critical-sized calvaria bone defect (Fig. S4 B), and monitored cell survival *in vivo* using AkaLuc fluorescence eight days post-implantation (Fig. 7 B).

Rats were euthanized at 6 weeks and 12 weeks after surgery

respectively. At 6 weeks, to assess cartilage formation, significant Safranin-O staining and Col-II expression were observed at the defect edges in both MSC-C and MSC-E4 groups, whereas barely no cartilage formation was noted in the control group (Fig. 7C & D). This indicates that endochondral bone formation relies on the presence of exogenous MSCs and scaffolds. Histological assessments at the 12-week disclosed a pronounced expression of Col-I in the MSC-E4 group. Despite similar densities of Col-I positive cells in the Ctrl and MSC-C groups, the relative bone thickness of defect area was significantly lower than both MSC-C and MSC-E4 groups. Within Masson's trichrome staining, newly formed collagens appeared blue, and newly formed mature bone appeared red. Notably, a more pronounced bone tissue formation was observed in the MSC-E4 group, consistent with Col-I expression (Fig. 7 E & F). Micro-CT scans of the calvarial defects demonstrated a substantial increase in bone volume fraction (BV/TV), bone mineral density (BMD), and the relative bone growth surface area (Fig. 7 G & H) in MSC-E4 group. Furthermore, a higher mineral apposition rate (MAR) was recorded in the MSC-E4 group compared to the control and MSC-C groups (Fig. 7 I & J), indicating that MSC-E4 with microscaffold
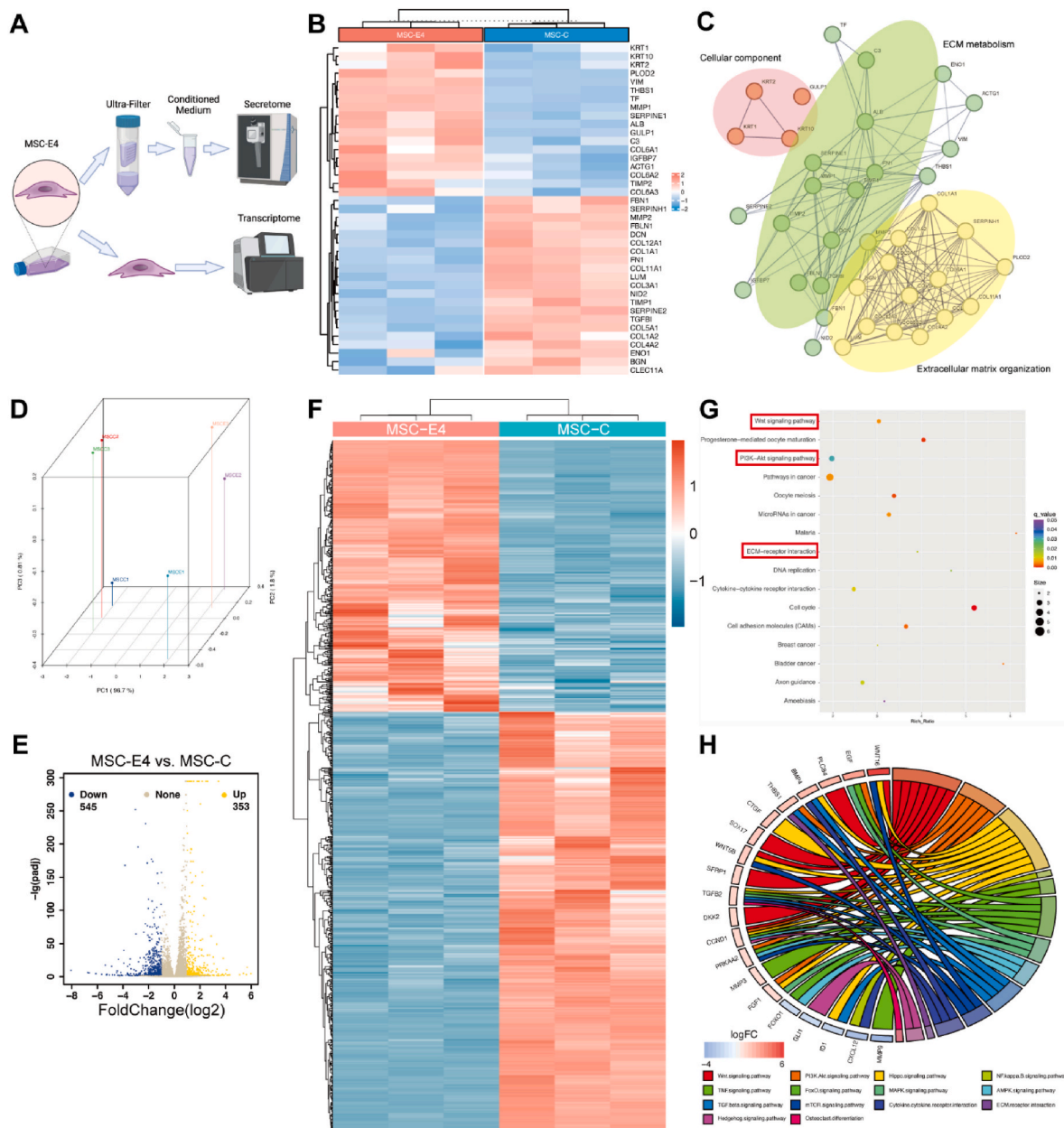
Fig. 3. Secretome and Transcriptome Analysis of MSC-E4. A) Schematic representation of secretome extraction from MSC-E4 via ultrafiltration and subsequent analysis through liquid chromatography-mass spectrometry (LC-MS), along with transcriptome sequencing workflow. B) Heatmap demonstrating the distinct protein expression profiles between MSC-E4 and MSC-C, as identified through secretome analysis. C) Protein-Protein Interaction (PPI) network visualizing the interplay among differentially expressed proteins, established using the STRING database. D) Principal Component Analysis (PCA) plot illustrating the global gene expression differences between MSC-E4 and MSC-C. E) Volcano plot illustrating the differential gene expression between MSC-C and MSC-E4 based on transcriptome data. F) Heatmap showcasing the differential gene expression patterns between MSC-E4 and MSC-C. G) Scatter plot highlighting the most significant pathways influenced by MSC-E4, determined through KEGG pathway enrichment analysis. H) Chord diagram elucidating the intricate relationships between various signaling pathways and their corresponding differentially expressed genes (DEGs) in MSC-E4.

facilitates bone defect repair by promoting endochondral ossification. To exclude the independent effects of the microscaffold, a vehicle group without cells was also examined, showing no significant differences in micro-CT parameters, quantitative measurements, or histological staining compared to the control group (Figure S4 C-E).

3. Discussion

In this study, we established an *in vitro* MSC-E4 ECO model to simulate the bone regeneration process, revealing both autocrine and paracrine roles in bone remodeling. MSC-E4 demonstrated superior

differentiation in chondrogenesis and hypertrophic conditions during ECO process, with an increased cell ratio in ECO cell fate, as shown by single-cell sequencing. In a rat critical-sized calvarial defect model, MSC-E4 encapsulated in microscaffolds effectively guided bone regeneration. Our findings suggest that MSC-E4 hold therapeutic promise for bone regeneration through ECO process.

3.1. GLP-1RA and bone regeneration

Past research on GLP-1R in bone metabolism primarily focused on its role in postprandial suppression of bone resorption, and studies have
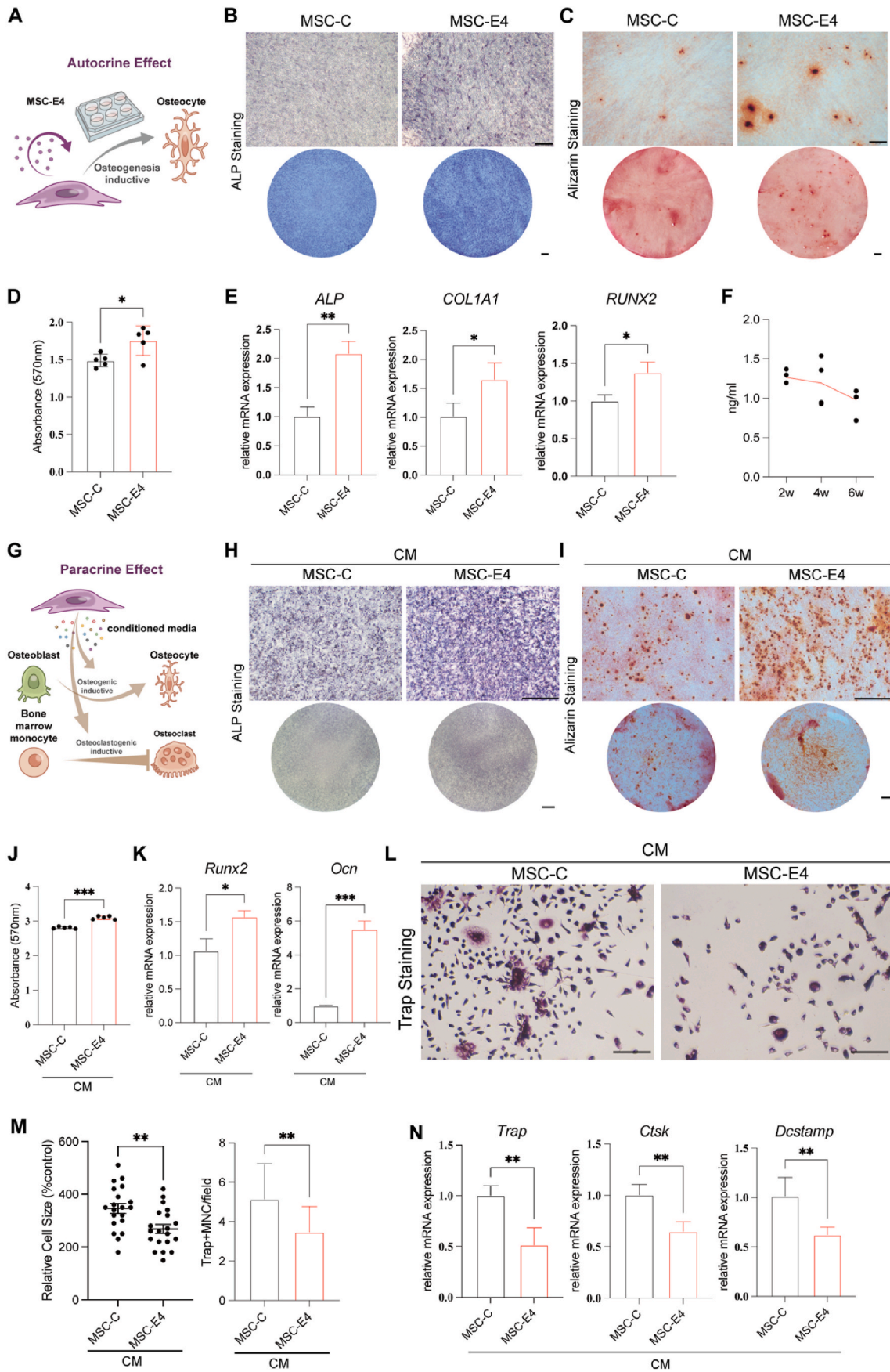
(caption on next page)

Fig. 4. Effects of MSC-E4 on autocrine and paracrine during bone remodeling. A) Schematic depicting the study of MSC-E4's autocrine effects on osteogenic function. B) ALP activity in MSCs following 7 days of osteogenic induction. C) Alizarin Red S staining of MSCs after 21 days of osteogenic induction. D) Quantification of MSC mineralization at 570 nm using a spectrophotometer. E) mRNA expression levels of osteogenic markers in MSCs at day 7 of osteogenesis. F) Excedin-4 expression in MSC medium during osteogenesis was tested via ELISA. G) Schematic illustrating the study of MSC-E4's paracrine effects on bone remodeling. H) ALP activity in MLO-A5 cells following 7 days of osteogenic induction. I) Alizarin Red S staining of MLO-A5 cells after 14 days of osteogenic induction. J) Mineralization of MLO-A5 cells measured at 570 nm with a spectrophotometer. K) mRNA expression of osteogenic markers in MLO-A5 cells at day 7 of osteogenesis. L) TRAP staining of mouse bone marrow macrophages (BMMs) during osteoclastogenesis. M) Quantitative analysis of relative cell size and number of Trap-positive multinucleated cells ($n \geq 3$) per field. N) mRNA expression levels of osteoclastogenesis markers in mBMMs. Scale bar, 200 μm. For all charts, data are presented as means ± SEM (standard error of the mean), *$p < 0.05$, **$p < 0.01$, ***$p < 0.01$, $n \geq 3$ per group.
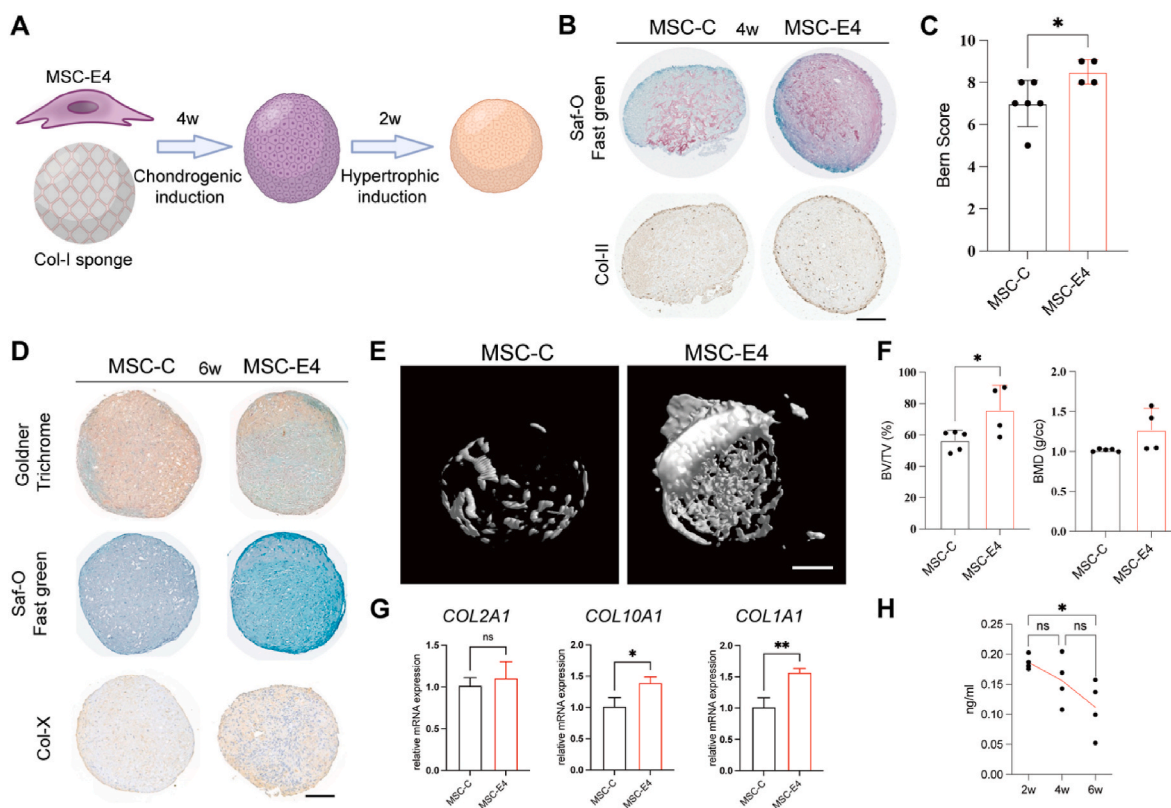
Fig. 5. Developing *in vitro* ECO Model. A) Schematic diagram of MSC-E4 in ECO *in vitro* model. B) Histological analysis at 4 weeks with Safranin-O staining and immunohistochemical detection of Col-II. C) Bern score evaluation of the neocartilage formed in the ECO model at 4 weeks. D) Histological assessment at 6 weeks with Goldner's trichrome, Safranin-O staining, and immunostaining for Col-X. E & F) Micro-CT results of (E) the 3D reconstruction figure and (F) parameters of the ECO model. G) mRNA expression of chondrogenic, hypertrophic and osteogenic collagen markers in ECO model. H) Excedin-4 expression in MSC-E4 CM during ECO, determined via ELISA. Scale bar, 200 μm *$p < 0.05$, **$p < 0.01$, $n \geq 3$ per group.

linked parenteral feeding to reduced bone mass and altered bone remodeling markers [23,47,48]. Clinical data indicate that GLP-1RA can enhance bone formation and modulate bone resorption in patients [49, 50]. Lower serum GLP-1 levels have been reported in elderly fracture patients compared to healthy adults [51]. Glp-1r -/- mice exhibited cortical osteopenia, diminished mechanical properties, a less mature collagen matrix, increased osteoclast numbers, and heightened resorption activity [24,25]. GLP-1 R A treatment in diabetic or hyperlipidemic animal models improved bone metabolic parameters and microarchitecture, suggesting GLP-1's potential anabolic effects on bone tissue independent of insulin [27–29,52]. GLP-1R expression has been confirmed in osteoblast and early osteocyte cell lines, and GLP-1RA has been shown to foster osteogenic differentiation via the cAMP-*p*-AMPK pathway [26] [27,53,54]. Additionally, GLP-1RA inhibits osteoclastogenesis [55]. The precise mechanisms of GLP-1RA's action on bone turnover remain unclear, with theories involving nervous, endocrine, or direct regulation of bone cells [23,56,57]. Exendin-4, identified from the Gila Monster's saliva in 1992, contrasts with human GLP-1's brief half-life due to its extended half-life of about 2.4 h [30,58,59]. This discovery led to the first FDA-approved GLP-1RA, Byetta, in 2005 [60].

However, for bone defect treatment spanning weeks, even this extended half-life is inadequate. Addressing this, we genetically engineered MSCs for prolonged Exendin-4 expression, enabling a deeper exploration of its bone repair mechanisms. Furthermore, the challenges of short half-life and targeted delivery in bone repair are addressed by our approach, where Exendin-4 modified MSCs foster bone remodeling and regeneration via endochondral ossification, overcoming the limitations of localized administration.

3.2. A newly designed ECO in vitro model aligned with BTE principles

The model we utilized was inspired by previously established models and involved a commercially available Col-I sponge [42–44], aligning well with BTE requirements including scaffolds, MSCs, and bioactive factors. Single-cell sequencing was employed to elucidate MSC cell clusters and fates within the ECO model, enhancing our understanding of *in vitro* ECO.

Single-cell sequencing identified four cell clusters—CPCs, ICs, RCs, and POs—within the ECO process. We observed two primary cell fates originating from CPCs: one leading to osteogenic differentiation (ECO
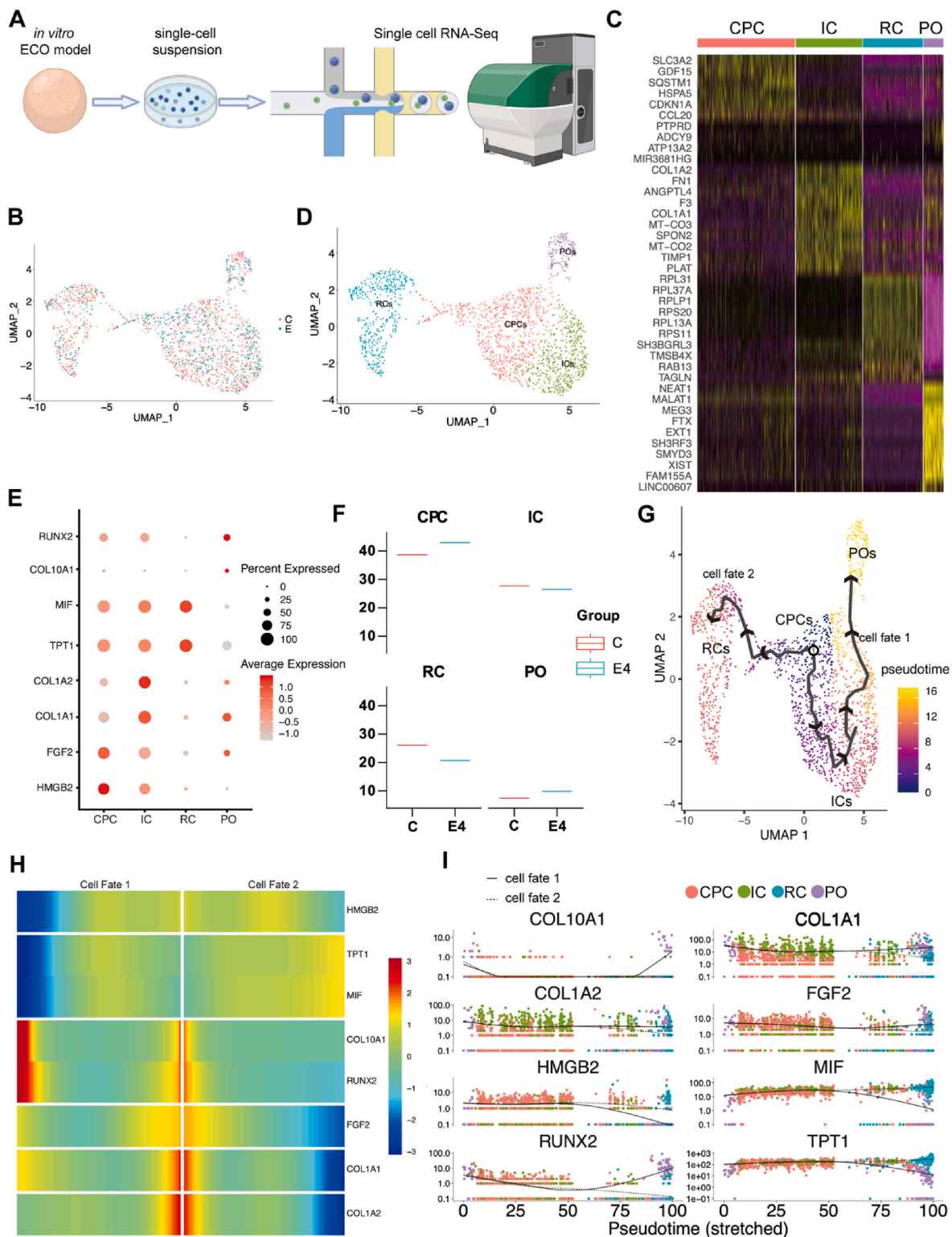
Fig. 6. Mechanism of MSC-E4 in ECO depicted by single-cell transcriptomic analysis. A) A schematic overview of the single-cell RNA sequencing process for MSC-E4 model. B) UMAP plot illustrating the transcriptomic landscape of both MSC-C and MSC-E4 cell populations. C) Heatmap presenting the top 10 differentially expressed genes (DEGs) across identified cell subsets. D) UMAP plot depicting the distribution of clustered cell populations. E) DotPlot highlighting specific marker genes characterizing the defined cell clusters. F) Comparative analysis of the distribution of cell clusters between the MSC-C and MSC-E4 groups. G) Developmental trajectory inferred by Monocle 3, showcasing potential lineage progression. H) Branched heatmap visualization of marker gene expression, delineating divergence into two cell fates. I) Expression profiles of marker genes associated with two distinct cell fates set against the backdrop of the various cell clusters.
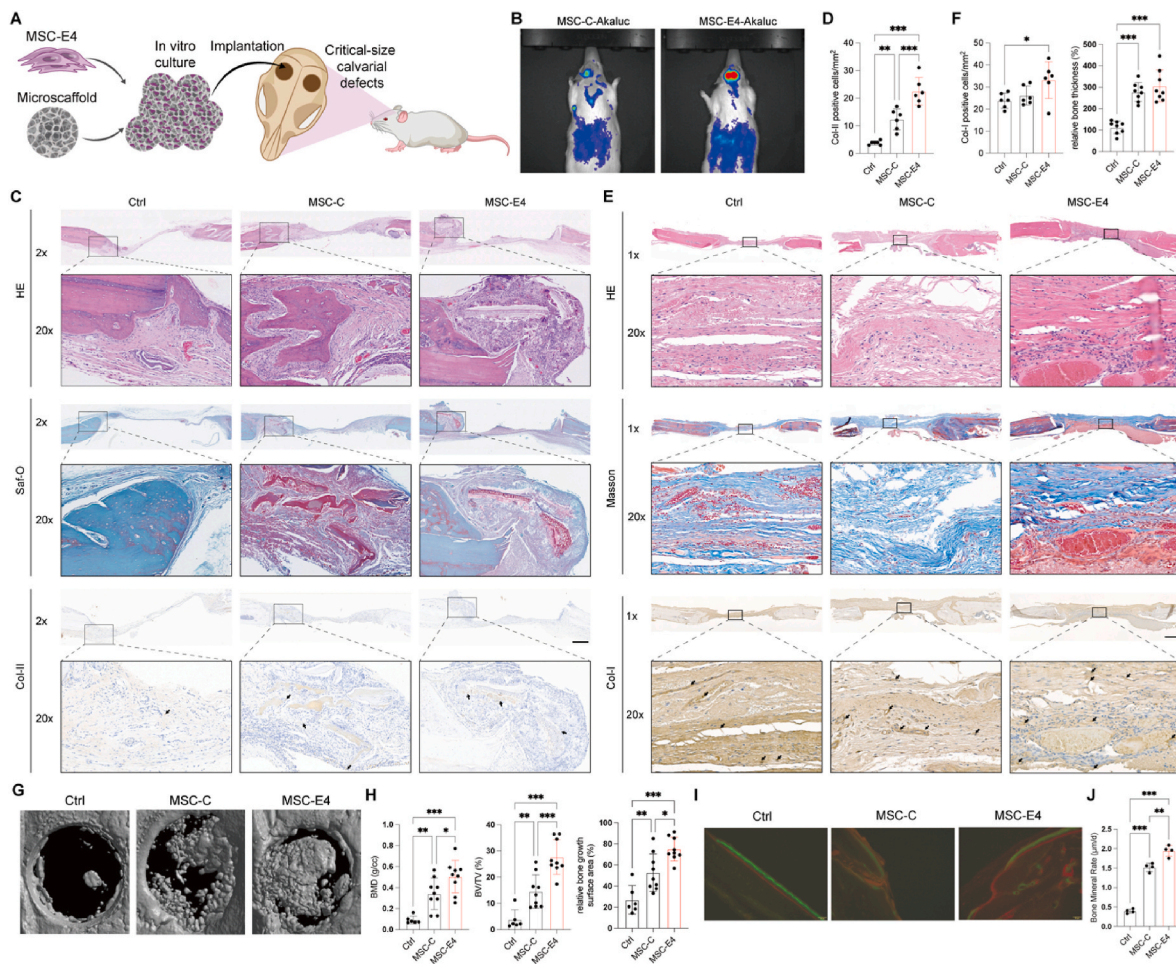
Fig. 7. Effects of MSC-E4 with Microscaffold for Bone Regeneration in Rat Critical-Sized Calvarial Defect Model. A) Schematic illustration of the *in vivo* rat calvarial critical-sized bone defect model. B) *in vivo* imaging displaying AkaLuc fluorescence. C) Histological sections stained with hematoxylin and eosin (H&E), Safranin-O (Saf-O), and Col-II, highlighting cartilage (indicated by black arrows) at 6 weeks post-implantation, the black arrows denote Col-II positive cells, scale bar, 500 μm. D) Quantification of Col-II positive cells. E) Histological sections stained with H&E, Masson's trichrome, and Col-I at 12 weeks post-implantation, the black arrows denote Col-I positive cells and relative bone thickness at 12 weeks post-implantation, scale bar, 500 μm. F) Quantification of Col-I positive cells and relative bone thickness at 12 weeks post-implantation. G) Three-dimensional reconstruction of regenerated bone via micro-CT. H) Analysis of bone mineral density (BMD), bone volume fraction (BV/TV), and relative bone growth surface area. I) Histological sections of calvaria labeled with calcein (green) and Alizarin Red S (red). Green denotes calcein injected 2 weeks prior to euthanasia; red indicates Alizarin Red S injected 3 days prior to euthanasia. J) Quantitative assessment of the mineral apposition rate (MAR), calculated as the average distance between two lines divided by the number of days, scale bar, 50 μm*$p < 0.05$, **$p < 0.01$, ***$p < 0.01$; $n \geq 3$ per group.

fate) and the other serving a regulatory function (RCs). MSC-E4 increased the proportion of cells in the ECO fate and decreased those in the regulatory role. Transcriptome and secretome analyses suggest that inflammatory cytokines early in ECO differentiation and subsequent pro-angiogenic factors are crucial [61–68]. Our findings indicate that the ECO model effectively evaluates the regenerative capabilities of MSC-E4.

4. Guiding bone regeneration with MSC-E4 and microscaffold

In the *in vivo* study, we used a rat critical-size calvarial defect model, which had been recently used in the study of endochondral osteogenesis [21,69–71]. Despite intramembranous ossification being the predominant process in calvarial development, the presence of cartilage has been documented in parietal bone regions [72]. Preclinical investigations have established that an *in vitro* ECO approach necessitates a Col-I sponge to foster MSC aggregation and maturation. Addressing the initial inflammatory response and cell migration at the defect site, as well as ectopic bone formation, our microscaffold served as a 3D microcarrier, enhancing cellular activity and targeted regenerative outcomes [14,16,37]. The cellular microcarriers, post-chondrogenic

induction, yielded a cartilaginous matrix within calvarial defects, whereas the absence of cells resulted in inadequate osteogenic recovery—a hallmark of critical-sized defects. The ECO-driven chondrogenesis and hypertrophic transitions were instrumental in bone repair [22,39,73], mirrored by marked chondrogenesis in the MSC-E4 group at 6 weeks, potentially pivotal to the overall healing process. Thus, our study establishes that MSC-E4, encapsulated in microscaffolds, efficaciously fosters bone regeneration via the ECO process.

4.1. Strengths and limitations

We elucidated MSC-E4's potential regulatory function in bone remodeling, characterized cell clustering and fate changes in the ECO model via single-cell sequencing, and enhanced bone regeneration in a rat model using MSC-E4 with microcarriers. Nonetheless, understanding the spatial cellular communication and structure during *in vitro* ECO is needed, and other factors like hydrostatic pressure [74], material stiffness, and porosity may influence ECO or differentiation, warranting further research. Challenges include ethical considerations in stem cell and gene therapies, potential immunogenic risks of human stem cell transplants, and costs related to cell transfection and microscaffold

cultivation.

On the positive side, this research aligns with BTE strategies, promising for bone disease treatment, especially bone defect repair. Additionally, our secretome analysis provides a foundation for further therapeutic developments, exploring the potential of extracellular secretome components.

5. Conclusion

In conclusion, MSC-E4 has been engineered and its role in modulating bone remodeling via autocrine and paracrine pathways has been validated. An *in vitro* MSC-E4 ECO model was used to simulate the bone regeneration process, showcasing enhanced differentiation during chondrogenesis and hypertrophic induction. Our innovative approach employed single-cell sequencing within the ECO model to delineate four distinct cell subsets, providing deeper insights into cellular fates during endochondral osteogenesis. Ultimately, we demonstrated that an ECO construct combining MSC-E4 with microscaffolds effectively orchestrates bone regeneration in a rat critical-sized calvarial defect model. This research paves the way for new bone defect treatments utilizing the principles of BTE with ECO constructs.

6. Materials and methods

6.1. Generation of MSC-E4

For the construction of recombinant cells, the Exendin-4 cDNA sequence (EU790959) from the Gila monster was sourced from the NCBI database. The coding sequence for Exendin-4 was: 5′-atgcatggtgaag-gaacatttaccagtgacttgtcaaaacagatggaa-gaggaggcagtgcggttatttattgagtggcttaa-gaacggaggaccaagtagcggggcacctccgccatcg-3′. This sequence was inserted into the lentiviral mammalian expression vector pLV-CMV-puro empty plasmids. Lentiviral particles were produced by co-transfecting the expression vector with the packaging vectors pVSVG and pΔ8.9 into 293 F T cells using the Neofect transfection agent (Neofect biotech). After 72 h, the supernatant was harvested and centrifuged at 19,500 rpm for 2.5 h to concentrate the viral particles, which were then reconstituted in Opti-MEM for infection of MSCs in the presence of polybrene (8 μg/ml) to enhance viral entry. Post-infection, cells were expanded to full confluence before passaging. Puromycin was introduced at 2.5 μg/ml to select stably transduced cells. The pcDNA3-Venus-Akaluc template was courtesy of Dr. Atsushi Miyawaki.

6.2. Cell culture and differentiation

MSCs was grown in αMEM (Gibco, Carlsbad, CA, USA) and contained 10 % FBS. MLO-A5 was grown in αMEM (Gibco, Carlsbad, CA, USA) and contained 5 % FBS and 5 % fetal calf serum. For osteogenesis differentiation, MSCs and MLO-A5s were treated with 500 μM ascorbic acid, 10 mM β-glycerophosphate, and 100 nM dexamethasone.

For osteoclasts differentiation, bone marrow-derived mononuclear cells (BMMs), isolated from the tibiae of 6-week-old male C57 mice, were cultured for 7 days in α-MEM supplemented with 10 % FBS and *M*-CSF (30 ng/ml, R&D). The cells were subsequently passaged and further cultured with *M*-CSF (30 ng/ml) and sRANKL (50 ng/ml, R&D) for approximately 5–7 days until multinucleated cell fusion was observed. Conditioned media from MSC-C (MSC-*C*-CM) or MSC-E4 (MSC-E4-CM) were added to the cultures at a 1:100 dilution in α-MEM. For TRAP staining, cells were fixed and stained to identify TRAP-positive multinucleated cells, which, possessing more than three nuclei, were quantified as osteoclasts based on size and number. Concurrently, mRNA was extracted to quantify genes associated with osteoclast differentiation.

6.3. H2O2 treatment

The antioxidant and antiaging responses of MSC-E4 were evaluated following H2O2 stimulation at a concentration of 100 μM. Cell viability was assessed using a CCK-8 kit (Dojindo, Japan) at 12 and 24 h post-treatment. At the 12-h mark, MSCs underwent TUNEL staining and were analyzed via FITC-PI flow cytometry (Beyotime Biotechnology, Beijing, China). Senescence was gauged using the Senescence β-Galactosidase Staining Kit (#C0602, Beyotime Biotechnology, Beijing, China), adhering to the provided protocol. Specifically, passage 7 MSCs were treated with 200 μM H2O2 for 6 h, followed by a period of incubation, and then β-galactosidase staining was performed for quantitative analysis.

6.4. Preparation of conditioned medium and secretome analysis

Cells were cultured in T75 flasks until they reached 80 % confluence. They were then rinsed with PBS and cultured for an additional 24 h in 8 ml of serum-free medium (NC0103, You Kang). The supernatant was then harvested, centrifuged, and passed through a 0.45-μm filter. CM was prepared by concentrating the filtered supernatant using ultrafiltration with an ultrafiltration tubes (Vivaspin Turbo 15 P ES, 3000 MWCO PES). The CM were then mixed with cold acetone (12,377, Tongguang Chem) in a ratio of 5:1 (v/v), followed by incubation at -20 °C. After 4 h of incubation, the samples were centrifuged at 7500 rpm for 20 min, and the supernatants were removed. The remaining protein pellets were collected and resuspended with 300 μl of 8 M urea buffer (BDH4602, VWR). Each 100 μg of proteins was reduced with dithiothreitol (D9760, Sigma-Aldrich), alkylated with iodoacetamide (I6125, Sigma-Aldrich), and digested with sequencing grade–modified trypsin (V5111, Promega). The resulted peptides solution was desalted with Sep-Pak C18 (Waters) and labeled with tandem mass tag reagent (Thermo Fisher Scientific). Then, the resulted peptides were divided into 12 fractions through first-dimension reverse phase liquid chromatography separation.

Liquid chromatography–tandem mass spectrometry (LC-MS/MS)–based quantitative secretome analysis was performed using Orbitrap Fusion Lumos mass spectrometer (Thermo Fisher Scientific) and online-coupled nano–high-performance liquid chromatography system (Thermo Fisher Scientific). Peptides were separated by gradient elution in elution buffer at a flow rate of 0.25 μl/min for 2 h, containing mobile phase A (0.1 % formic acid in water) and mobile phase B (0.1 % formic acid in acetonitrile). The mass spectrometer with Xcalibur software (version 3.0) was fixed to data-dependent acquisition mode, followed by the acquisition of full-scan mass spectrum. Data-dependent MS2 scans were performed 20 times at higher-energy collisional-based fragmentation. Data of each LC-MS/MS run were examined through the SEQUEST search engine from Proteome Discoverer software (version 2.1, Thermo Fisher Scientific) against the UniProt database.

6.5. Exendin-4 concentration measurement

The concentration of Exendin-4 in the supernatant and exosomes was quantified 24 h post-construction using an exenatide ELISA kit (EK-070-94, Phoenix Pharmaceuticals), with values calculated against Exendin-4 standard curves. Samples were collected for analysis at three key time points—2, 4, and 6 weeks—during both osteogenic and ECO induction phases.

6.6. RNA extraction and RT-qPCR

Total RNA was extracted from the cultured cells, villous tissues, and placental tissues using Simply P Total RNA (Bioer, Hangzhou) according to the manufacturer's instructions. The RNA concentration was measured by ultraviolet spectroscopy (Microdrop; Bio-DL Corporation). Total RNA (1 μg) was used for reverse transcription with a Prime Script

RT reagent kit (Takara Bio). Primers were synthesized by Sangon Biotech; GAPDH was used as an endogenous control for gene expression analysis. The sequences of the PCR primer pairs for each gene are shown in Table 1. Quantitative RT-PCR was carried out using a Bio-Rad CFX Connect Detection System (Bio-Rad, Hercules, USA). PCR cycling conditions included predenaturing at 95 °C for 3 min, followed by 40 cycles (94 °C for 5 s, 58 °C for 15 s, and 72 °C for 15 s) and extension at 72 °C for 30 s. The threshold cycle Ct value was defined as the fractional cycle number at which the fluorescence passed the fixed threshold.

6.7. RNA sequencing

RNA-seq analysis was conducted on MSC-C and MSC-E4, using 1 μg of total RNA for each sample. RNA-seq was conducted by Anoroad Gene Technology (Beijing, China). Differential expression genes were identified by the DESeq2 package, and functional enrichment for GO and KEGG was performed with the GOstats package.

6.8. Western blots

Briefly, cells or tissues were homogenized in radio-immunoprecipitation assay buffer (PS0012, Leagene). Protein concentrations were determined using the BCA Protein Assay Kit (P0010S, Beyotime). Samples were loaded on 10 % SDS–polyacrylamide gel electrophoresis gels and then transferred to nitrocellulose membranes. Immunoblotting was done in primary antibody dilution buffer (A1810, Solarbio) with the corresponding antibodies. The antibodies were purchased as follows: anti–GLP–1R (bs-1559 R, Bioss) and anti–GAPDH (881, YEASEN).

6.9. Endochondral ossification (ECO) induction protocol

Drawing on methodologies from prior *in vitro* research [42–44], we encapsulated MSCs within COL-I sponges (Collagen Sponge, Bonanga) fashioned to 2.5 mm in diameter and 5 mm in height. P7 MSC-C or MSC-E4 cells were resuspended and seeded into the scaffolds at a volume of 12.5 μl and concentration of 40,000 cells/μl. The cultures were maintained with bi-daily replacement of the ECO induction medium. This induction involved two distinct phases: chondrogenesis followed by

hypertrophy. The chondro-inductive medium was composed of 10 ng/ml TGF-β3 (P02149, Solarbio), 100 nM dexamethasone (Sigma-Aldrich), and 10 μM ascorbic acid (Sigma-Aldrich). The hyperchondro-inductive medium included 50 μM L-thyroxin (IT0210, Solarbio), 100 nM dexamethasone, 50 pg/ml interleukin 1-β (Solarbio), and 0.01 M β-glycerolphosphate (Sigma-Aldrich).

6.10. Morphological observation of microscaffolds

The architecture of the microscaffolds (3D TableTrix® Microcarriers, CytoNiche Biotech, Beijing) was scrutinized using scanning electron microscopy (SEM, JSM-7900 F, Japan). This was performed both in the presence and absence of MSC cultures. The microscaffolds were subjected to freeze-drying, followed by a 90-s gold sputter coating to enhance electrical conductivity prior to SEM imaging, facilitating detailed microstructural assessment.

6.11. Establishment of critical-size rat calvarial defect and MSC implantation

The rat calvarial defect model and subsequent animal experiments were conducted under the approval of the Peking University Ethics Committee (LA2019365). Forty male Sprague-Dawley (SD) rats, aged 8 weeks and weighing 220–240 g, were acclimatized to specific-pathogen-free conditions with ad libitum access to food and water, and a controlled 12-h light/dark cycle, before the experiments began. After a week of acclimatization, rats were randomized into four groups (n = 10 each): control, cell-free microscaffold (Vehicle), MSC-C with microscaffold (MSC-C), and MSC-E4 with microscaffold (MSC-E4). Under isoflurane anesthesia and semi-sterile conditions, a longitudinal incision was made on the scalp, followed by periosteal dissection. A 5 mm diameter defect was carefully created using a trephine bur, with continuous saline irrigation to reduce heat injury. The dura mater was meticulously preserved to prevent hemorrhage and ensure optimal bone healing conditions. The respective group implants were placed into the defects, and the surgical site was closed with sutures. Post-operative care included the administration of 100 mg/kg cefazolin for two days to prevent infection.

6.12. Micro-CT scanning and analysis

Twelve weeks post-operation, rats were euthanized with carbon dioxide. The excised calvarial specimens, encompassing the defect area, were fixed in 4 % paraformaldehyde for 24 h. Subsequently, they were assessed using micro-CT (SCANCO μCT-100, Switzerland). Parameters including bone volume/tissue volume (BV/TV), bone mineral density (BMD), and the relative bone growth surface area of the regenerated tissue were quantified using the Evaluation V6.5 software (SCANCO, Switzerland).

6.13. Histology and immunohistochemistry

Histological and immunohistochemical examinations were performed on both *in vitro* ECO model and *in vivo* calvarial samples. The calvarial specimens were decalcified using 10 % EDTA solution over a period of four weeks. Following a sequential dehydration process in graded ethanol series, the samples were embedded in paraffin at a section thickness of 7 mm. Staining was carried out with hematoxylin and eosin (H&E), Safranin O, Alcian blue, and Masson's trichrome. For immunohistochemical analysis, antibodies targeting Col-I (Novus, NB600-408, 1:100), Col-II (bs-10589R, 1:200), and Col-X (eBioscience, 14-9771-82, 1:200) were employed. The neocartilage, developed through the ECO process *in vitro*, was quantitatively assessed using the Bern Score [75].

Table 1
Primer list.

Primer name	Sequence (5′ to 3′)
h-Exendin-4-F	CGCTCTAGAATGCATGGTGAAGGAACATTTAC
h-Exendin-4-R	CGCGGATCCTTACGATGGCGGAGGTGCCCCGC
h-ALP-F	ACCACCACGAGAGTGAACCA
h-ALP-R	CGTTGTCTGAGTACCAGTCCC
h-COL1A1-F	ATGTTCAGCTTTGTGGACCTC
h-COL1A1-R	CTGTACGCAGGTGATTGGTG
h-Runx2-F	TGGTTACTGTCATGGCGGGTA
h-Runx2-R	TCTCAGATCGTTGAACCTTGCTA
h-COL2A1-F	TGGACGATCAGGCGAAACC
h-COL2A1-R	GCTGCGGATGCTCTCAATCT
h-COL10A1-F	ATGCTGCCACAAATACCCTTT
h-COL10A1-R	GGTAGTGGGCCTTTTATGCCT
h-GAPDH-F	AGGTCGGTGTGAACGGATTTG
h-GAPDH-R	GGGGTCGTTGATGGCAACA
m-Runx2-F	AACGATCTGAGATTTGTGGGC
m-Runx2-F	CCTGCGTGGGATTTCTTGGTT
m–OCN–F	AGGGAGGATCAAGTCCCG
m–OCN–R	GAACAGACTCCGGCGCTA
m-Trap-F	CACTCCCACCCTGAGATTTGT
m-Trap-R	CCCCAGAGACATGATGAAGTCA
m-Ctsk-F	CTCGGCGTTTAATTTGGGAGA
m-Ctsk-R	TCGAGAGGGAGGTATTCTGAGT
m-Dcstamp-F	GGGGACTTATGTGTTTCCACG
m-Dcstamp-R	ACAAAGCAACAGACTCCCAAAT
m-GAPDH-F	CAGTGCCAGCCTCGTCCCGTAGA
m-GAPDH-R	CTGCAAATGGCAGCCCTGGTGAC

6.14. Bone histomorphometry analysis

For mineralization rate analysis, alizarin red (30 mg/kg, Sigma-Aldrich, United States) and calcein (30 mg/kg, Sigma-Aldrich, United States) with fluorescent labeling were injected intraperitoneally at 3 and 21 days before euthanasia, respectively. Sample collection and histological processing were performed as described above. Non-decalcified sections were observed using a fluorescence microscope (Olympus, Japan).

6.15. Single-cell RNA-seq library preparation and sequencing

Preparation and quality control of the single-cell suspension: MSC microspheres (n = 5 for each group) cultured for 6 weeks *in vitro* for endochondral induction, then placed in complete medium containing 0.1 % type I Collagenase degradation in 37 °C constant temperature shaking table at a speed of 40 rpm for 1 h. The cell dissociation solution was filtered through a 40 μm cell strainer, centrifuged at 400 g, resuspended in 1 ml PBS containing 0.04 % BSA, and washed twice. Subsequently, an appropriate amount of PBS was added to the cell precipitate to obtain a single-cell suspension at a concentration close to the target value. The single-cell suspension was then inspected for cell quality. Once high activity (>85 %), less agglomeration, a clean background, and an appropriate concentration were obtained, the sample was immediately placed on ice for subsequent use.

Construction, quality control, and sequencing of the library: After obtaining a qualified single-cell suspension, water in the oil drop library was prepared through a microfluidic channel. A single gel bead and single cell were first wrapped by separate water-in-oil droplets to form gel bead-in-emulsions (GEMs). Each gel bead had a unique barcode, unique molecular identifier (UMI) sequence, and poly-dT primer sequence for the reverse transcription reaction. Subsequently, in the GEM reaction system, the cells were lysed, mRNA was released, and the reverse transcription reaction was initiated with the poly-dT primer sequence using reverse transcriptase to produce the first-strand cDNA. The first-strand cDNA was then enriched by PCR amplification and the library was constructed. Library concentration was then measured using a nucleic acid quantitative analyzer (Qubit® 3.0, Life Technologies, Carlsbad, USA), and a highly sensitive DNA detection kit (Agilent Technologies, Santa Clara, USA) was used to determine the length distribution of the library fragments. Quantitative PCR (qPCR) was used to quantify the effective concentration of the library, expected as greater than 10 nmol/L. After the qualified library was prepared, it was sequenced using an Illumina HiSeq platform (San Diego, USA).

Data quality control: Bcl2fastq2 (v2.18, Illumina) was used to extract data and generate FASTQ files for each cell using unique barcode combinations in the Nextera XT DNA Library. The FASTQ files of the 12 samples were processed using Cell Ranger (v3.1.0) and sus scrofa (pig) Sscrofa11.1.90 chromosome was used as the reference genome in Cell Ranger to generate the feature barcode matrix. Next, the Seurat object list was generated using the Seurat package (v. 3.2.0) 7, 41 with R software (v.3.5.1) according to the following criteria: (1) minimum cells = 5; (2) 800 < nFeature_RNA <10,000; (3) percentage mt < 0.2. In other words, genes expressed in at least 5 cells and cells detected gene number ranged from 800 to 10,000 were kept for further analysis. Low-quality cells were also filtered if ≥ 20 % UMIs derived from the mitochondrial genome. Doublet cells were evaluated using Scrublet 49 and were removed in the following analysis.

Data dimensionality reduction: The filtered gene matrix was normalized using the NormalizeData function, and 2000 variable genes with high intercellular variation were analyzed using the FindVariableFeatures function 30. To reduce the dimensionality of the datasets, the RunPCA function was executed with default parameters on linear transformation-scaled data generated by the ScaleData function. To eliminate batch effects across samples, the first 20 dimensions of canonical correlation analysis (CCA) and principal component analysis

(PCA) were used. Cells were clustered using the FindNeighbors and FindClusters functions (0.1 resolution setting) and UMAP (Uniform Manifold Approximation and Projection) visualization was performed with the first 20 dimensions.

Identification of cell subsets and marker genes: Clusters were classified and annotated based on the expression of canonical markers of particular cell types. Correlation analysis between clusters and Single R score were used to distinguish chondrocyte subsets from non-chondrocyte subsets. Based on the conclusions of previous studies, functional enumeration analysis was used to assist in identifying cell subsets. Markers for each of the identified clusters were identified using the FindAllMarkers function of Seurat. Additionally, an R package SingleR was used as a reference-based single-cell RNA-Seq annotation tool, and the human BlueprintEncodeData dataset was chosen as references by using homologous genes.

DEG identification and functional enrichment analysis: the FindMarkers function of Seurat was used to identify differentially expressed genes (DEGs) between two groups of cells with default parameters (logfc.threshold = 0.25, test. use = "wilcox," min. pct = 0.1, p_val_adj <0.01). We performed Gene Ontology (GO) and Kyoto Encyclopedia of Genes and Genomes (KEGG) functional enrichment analyses with hypergeometric tests. Enrichment terms were obtained with p. adjust <0.05. *P*-value adjustment (FDR) was performed using the Benjamini-Hochberg method.

Single-cell trajectory analysis: By studying the gene expression changes of each cell, we analyzed the overall gene trajectory to place each cell in the appropriate position in the trajectory and obtain the arrangement relationships between cell subsets. Single-cell trajectory analysis was performed using Monocle 2 with DDRTree dimensionality reduction and default parameters 36. The raw expression counts of cells were filtered. Branch expression analysis modelling (BEAM) was performed for branch fate-determined gene analysis. Using scRNA-seq data, the dynamic change direction and rate for the whole transcriptome were inferred by the accurate and sensitive detection of RNA abundance signals.

6.16. Statistical analysis

Data are expressed as mean ± SEM. Statistical comparisons for two groups were made using unpaired Student's t-test, while one-way ANOVA was employed for multiple group analyses, followed by post-hoc tests for detailed pairwise comparisons. These analyses were conducted using GraphPad Prism software (version 9.5; La Jolla, California, USA). For ANOVA, post-hoc comparisons were performed using Tukey's multiple comparisons test, as appropriate, to adjust for multiple testing. A p-value of less than 0.05 was deemed to indicate statistical significance.

Ethics approval

The procedures that involved the use of animals for the rat calvarial defect experiment were approved by the ethics committee of Peking University (LA2019365).

CRediT authorship contribution statement

Zihao He: Writing – review & editing, Writing – original draft, Methodology, Investigation, Formal analysis. **Hui Li:** Writing – review & editing, Funding acquisition, Formal analysis, Conceptualization. **Yuanyuan Zhang:** Resources, Methodology. **Shuang Gao:** Resources, Methodology. **Kaini Liang:** Visualization, Methodology. **Yiqi Su:** Methodology. **Yanan Du:** Validation, Supervision, Conceptualization. **Du Wang:** Methodology. **Dan Xing:** Writing – review & editing, Writing – original draft, Visualization, Supervision, Funding acquisition, Formal analysis, Conceptualization. **Zhen Yang:** Methodology. **Jianhao Lin:** Supervision, Project administration, Data curation, Conceptualization.

Declaration of generative AI and AI-assisted technologies in the writing process

During the preparation of this work, the author(s) used ChatGPT to improve the language. After using this tool/service, the author(s) reviewed and edited the content as needed and take(s) full responsibility for the content of the publication.

Declaration of competing interest

The authors declare the following financial interests/personal relationships which may be considered as potential competing interests: Jianhao Lin reports financial support was provided by Beijing Science and Technology Planning Project. Dan Xing reports financial support was provided by Beijing Natural Science Foundation. Dan Xing reports financial support was provided by National Natural Science Foundation of China.

Acknowledgments

Appendix A. Supplementary data

Supplementary data to this article can be found online at https://doi.org/10.1016/j.bioactmat.2023.12.007.

References

[1] Ismailidis, P., et al., Scope and limits of teriparatide use in delayed and nonunions: a case series. Clin. Practice. 11(1): p. 47-57..

[2] Hak, D.J., et al., Delayed union and nonunions: epidemiology, clinical issues, and financial aspects. Injury. 45 Suppl 2: p. S3-S7..

[3] Lerner, R.K., et al., Quality of life assessment of patients with posttraumatic fracture non union, chronic refractory osteomyelitis, and lower-extremity amputation. Clin. Orthop. Relat. Res., (295): p. 28-36..

[4] Trejo-Iriarte, C.G., et al., Evaluation of bone regeneration in a critical size cortical bone defect in rat mandible using microCT and histological analysis. Arch. Oral Biol.. 101: p. 165-171..

[5] Nicholson, J.A., et al., Fracture nonunion in long bones: a literature review of risk factors and surgical management. Injury. 52 Suppl 2: p. S3-S11..

[6] Qi, J., et al., Current biomaterial-based bone tissue engineering and translational medicine. Int. J. Mol. Sci.. 22(19): p. 10233..

[7] Ho-Shui-Ling, A., et al., Bone regeneration strategies: engineered scaffolds, bioactive molecules and stem cells current stage and future perspectives. Biomaterials. 180: p. 143-162..

[8] Koons, G.L., M. Diba, and A.G. Mikos, Materials design for bone-tissue engineering. Nat. Rev. Mater.. 5(8): p. 584-603..

[9] Fu, J., et al., Systemic therapy of MSCs in bone regeneration: a systematic review and meta-analysis. Stem Cell Res. Ther., 2021. 12(1): p. 377..

[10] Bunpetch, V., et al., Strategies for MSC expansion and MSC-based microtissue for bone regeneration. Biomaterials. 196: p. 67-79..

[11] Freitas, J., et al., Genetically engineered-MSC therapies for non-unions, delayed unions and critical-size bone defects. Int. J. Mol. Sci.. 20(14): p. 3430..

[12] Zhou, T., et al., Challenges and advances in clinical applications of mesenchymal stromal cells. J. Hematol. Oncol.. 14(1): p. 24..

[13] Moysidou, C.-M., C. Barberio, and R.M. Owens, Advances in engineering human tissue models. Front. Bioeng. Biotechnol.. 8: p. 620962..

[14] Xing, D., et al., Engineering 3D functional tissue constructs using self-assembling cell -laden microniches. Acta Biomater.. 114: p. 170-182..

[15] Li, H., et al., Self-assembled microtissues loaded with osteogenic MSCs for in vivo bone regeneration. Front. Bioeng. Biotechnol.. 10: p. 1069804..

[16] Wang, B., et al., A low dose cell therapy system for treating osteoarthritis: in vivo study and in vitro mechanistic investigations. Bioact. Mater.. 7: p. 478-490..

[17] Salhotra, A., et al., Mechanisms of bone development and repair. Nat. Rev. Mol. Cell Biol.. 21(11): p. 696-711..

[18] Stegen, S., et al., HIF-1α metabolically controls collagen synthesis and modification in chondrocytes. Nature. 565(7740): p. 511-515..

[19] Fu, R., et al., Bone defect reconstruction via endochondral ossification: a developmental engineering strategy. J. Tissue Eng.. 12: p. 20417314211004211..

[20] Bernhard, J., et al., Tissue-engineered hypertrophic chondrocyte grafts enhanced long bone repair. Biomaterials. 139: p. 202-212..

[21] Zhang, X., et al., *Msx1⁺* stem cells recruited by bioactive tissue engineering graft for bone regeneration. Nat. Commun.. 13(1): p. 5211..

[22] Zhang, M., et al., Recapitulation of cartilage/bone formation using iPSCs via biomimetic 3D rotary culture approach for developmental engineering. Biomaterials. 260: p. 120334..

[23] Helsted, M.M., et al., The role of endogenous GIP and GLP-1 in postprandial bone homeostasis. Bone. 140: p. 115553..

[24] Yamada, C., et al., The murine glucagon-like peptide-1 receptor is essential for control of bone resorption. Endocrinology. 149(2): p. 574-579..

[25] Mabilleau, G., et al., Optimal bone mechanical and material properties require a functional glucagon-like peptide-1 receptor. J. Endocrinol.. 219(1): p. 59-68..

[26] Nuche-Berenguer, B., et al., Presence of a functional receptor for GLP-1 in osteoblastic cells, independent of the cAMP-linked GLP-1 receptor. J. Cell. Physiol.. 225(2): p. 585-592..

[27] Kim, J.-Y., et al., Exendin-4 increases bone mineral density in type 2 diabetic OLETF rats potentially through the down-regulation of SOST/sclerostin in osteocytes. Life Sci.. 92(10): p. 533-540..

[28] Nuche-Berenguer, B., et al., Effect of GLP-1 treatment on bone turnover in normal, type 2 diabetic, and insulin-resistant states. Calcif. Tissue Int., 2009. 84(6): p. 453-461..

[29] Nuche-Berenguer, B., et al., GLP-1 and exendin-4 can reverse hyperlipidic-related osteopenia. J. Endocrinol.. 209(2): p. 203-210..

[30] Ma, X., et al., Exendin-4, a glucagon-like peptide-1 receptor agonist, prevents osteopenia by promoting bone formation and suppressing bone resorption in aged ovariectomized rats. J. Bone Miner. Res. : Off. J. Am. Soc. Bone Mineral Res.. 28(7): p. 1641-1652..

[31] Sun, H.-X., et al., The bone-preserving effects of exendin-4 in ovariectomized rats. Endocrine. 51(2): p. 323-332..

[32] Y. Sun, et al., Liraglutide promotes osteoblastic differentiation in mc3t3-E1 cells by ERK5 pathway, Int. J. Endocrinol. (2020), 8821077.

[33] Pal, S., et al., The osteogenic effect of liraglutide involves enhanced mitochondrial biogenesis in osteoblasts. Biochem. Pharmacol.. 164: p. 34-44..

[34] Zhai, S., et al., Glucagon-like peptide-1 receptor promotes osteoblast differentiation of dental pulp stem cells and bone formation in a zebrafish scale regeneration model. Peptides. 163: p. 170974..

[35] Wu, X., et al., Liraglutide, a glucagon-like peptide-1 receptor agonist, facilitates osteogenic proliferation and differentiation in MC3T3-E1 cells through phosphoinositide 3-kinase (PI3K)/protein kinase B (AKT), extracellular signal-related kinase (ERK)1/2, and cAMP/protein kinase A (PKA) signaling pathways involving β-catenin. Exp. Cell Res.. 360(2): p. 281-291..

[36] Zhang, Y.S., et al., Glucagon-like peptide-1 receptor agonists and fracture risk: a network meta-analysis of randomized clinical trials. Osteoporos. Int. : J. Established as Result of Cooperation Between the European Foundation for Osteoporosis and the National Osteoporosis Foundation of the USA. 29(12): p. 2639-2644..

[37] Zhang, Y., et al., Exendin-4 gene modification and microscaffold encapsulation promote self-persistence and antidiabetic activity of MSCs. Sci. Adv.. 7(27): p. eabi4379..

[38] Folkesson, E., et al., Differential protein expression in human knee articular cartilage and medial meniscus using two different proteomic methods: a pilot analysis. BMC Muscoskel. Disord.. 19(1): p. 416..

[39] Pigeot, S., et al., Manufacturing of human tissues as off-the-Shelf grafts programmed to Induce regeneration. Advanced materials (Deerfield Beach, Fla.). 33(43): p. e2103737..

[40] Gadjanski, I., K. Spiller, and G. Vunjak-Novakovic, Time-dependent processes in stem cell-based tissue engineering of articular cartilage. Stem cell Reviews Rep.. 8(3): p. 863-881..

[41] Dessau, W., et al., Changes in the patterns of collagens and fibronectin during limb-bud chondrogenesis. J. Embryol. Exp. Morphol.. 57: p. 51-60..

[42] Scotti, C., et al., Engineering of a functional bone organ through endochondral ossification. Proc. Natl. Acad. Sci. USA. 110(10): p. 3997-4002..

[43] Osinga, R., et al., Generation of a bone organ by human adipose-derived stromal cells through endochondral ossification. Stem Cells Transl. Med.. 5(8): p. 1090-1097..

[44] Guerrero, J., et al., Fractionated human adipose tissue as a native biomaterial for the generation of a bone organ by endochondral ossification. Acta Biomater.. 77: p. 142-154..

[45] Morimoto, Y., et al., TPT1 supports proliferation of neural stem/progenitor cells and brain tumor initiating cells regulated by macrophage migration inhibitory factor (MIF). Neurochem. Res.. 47(9): p. 2741-2756..

[46] Aghajanian, P. and S. Mohan, The art of building bone: emerging role of chondrocyte-to-osteoblast transdifferentiation in endochondral ossification. Bone Res.. 6: p. 19..

[47] Clowes, J.A., S. Khosla, and R. Eastell, Potential role of pancreatic and enteric hormones in regulating bone turnover. J. Bone Miner. Res. : Off. J. Am. Soc. Bone Mineral Res.. 20(9): p. 1497-1506..

[48] Jensen, N.W., et al., Associations between postprandial gut hormones and markers of bone remodeling. Nutrients. 13(9): p. 3197..

[49] Iepsen, E.W., et al., GLP-1 receptor agonist treatment increases bone formation and prevents bone loss in weight-reduced obese women. J. Clin. Endocrinol. Metabol.. 100(8): p. 2909-2917..

[50] Bergmann, N.C., et al., Separate and combined effects of GIP and GLP-1 infusions on bone metab olism in overweight men without diabetes. J. Clin. Endocrinol. Metabol.. 104(7): p. 2953-2960..

[51] Pazarci, Ö., et al., Evaluation of serum glucagon-like peptide 1 and vitamin D levels in el derly patients with bone fractures. Med. Princ. Pract. : Int. J. Kuwait Univ., Health Sci. Centre. 29(3): p. 219-224..

[52] Nuche-Berenguer, B., et al., Exendin-4 exerts osteogenic actions in insulin-resistant and type 2 di abetic states. Regul. Pept.. 159(1–3): p. 61-66..

[53] Zeng, Z., et al., MiR-27a-3p targets GLP1R to regulate differentiation, autophagy, and R elease of inflammatory factors in pre-osteoblasts via the AMPK signaling pathway. Front. Genet.. 12: p. 783352..

[54] Pacheco-Pantoja, E.L., et al., Receptors and effects of gut hormones in three osteoblastic cell lines. BMC Physiol.. 11: p. 12..

[55] Li, Z., et al., Liraglutide, a glucagon-like peptide-1 receptor agonist, suppresses os teoclastogenesis through the inhibition of NF-κB and MAPK pathways via GLP-1R. Biomed. & Pharmacother. = Biomed. & Pharmacother.. 130: p. 110523..

[56] Zhang, L., et al., Relationship between glucagon-like peptide-1 receptor gene polymorphis m and bone mineral density in postmenopausal women in Shanghai. Ann. Palliat. Med.. 9(4): p. 1732-1741..

[57] Kitaura, H., et al., Effects of incretin-related diabetes drugs on bone formation and bone resorption. Int. J. Mol. Sci.. 22(12): p. 6578..

[58] Raufman, J.P., et al., Truncated glucagon-like peptide-1 interacts with exendin receptors on dispersed acini from Guinea pig pancreas. Identification of a mammalia n analogue of the reptilian peptide exendin-4. J. Biol. Chem.. 267(30): p. 21432-21437..

[59] Eng, J., et al., Isolation and characterization of exendin-4, an exendin-3 analogue, fr om Heloderma suspectum venom. Further evidence for an exendin receptor on dispersed acini from Guinea pig pancreas. J. Biol. Chem.. 267(11): p. 7402-7405..

[60] Nauck, M.A., et al., GLP-1 receptor agonists in the treatment of type 2 diabetes - state-of -the-art. Mol. Metabol.. 46: p. 101102..

[61] De Spiegelaere, W., et al., Detection of hypoxia inducible factors and angiogenic growth factors d uring foetal endochondral and intramembranous ossification. Anat. Histol. Embryol. 39(4): p. 376-384..

[62] Kovacevic, A., et al., Expression of serum amyloid A transcripts in human bone tissues, diffe rentiated osteoblast-like stem cells and human osteosarcoma cell lines. J. Cell. Biochem.. 103(3): p. 994-1004..

[63] Lu, J.F., et al., Camptothecin effectively treats obesity in mice through GDF15 inductio n. PLoS Biol.. 20(2): p. e3001517..

[64] Mazor, R., et al., Matrix metalloproteinase-1-mediated up-regulation of vascular endothel ial growth factor-2 in endothelial cells. J. Biol. Chem.. 288(1): p. 598-607..

[65] Bertrand-Philippe, M., et al., Regulation of tissue inhibitor of metalloproteinase 1 gene transcripti on by RUNX1 and RUNX2. J. Biol. Chem.. 279(23): p. 24530-24539..

[66] Saw, S., et al., Metalloprotease inhibitor TIMP proteins control FGF-2 bioavailability and regulate skeletal growth. J. Cell Biol.. 218(9): p. 3134-3152..

[67] Salmi, A., et al., An integrative bioinformatics approach to decipher adipocyte-induced t ransdifferentiation of osteoblast. Genomics. 114(4): p. 110422..

[68] Li, J., et al., Exendin-4 regulates pancreatic ABCA1 transcription via CaMKK/CaMKIV pa thway. J. Cell Mol. Med.. 14(5): p. 1083-1087..

[69] Xing, Z., et al., Endochondral ossification induced by cell transplantation of endotheli al Cells and bone marrow stromal cells with copolymer scaffold using a rat calvarial defect model. Polymers. 13(9): p. 1521..

[70] Thompson, E.M., et al., An endochondral ossification-based approach to bone repair: chondrogen ically primed mesenchymal stem cell-laden scaffolds support greater Re pair of critical-sized cranial defects than osteogenically stimulated constructs in vivo. Tissue Eng. 22(5–6): p. 556-567..

[71] Morimoto, S., et al., *A Cartilaginous Construct With Bone Collar Exerts Bone-Regenerative Pr operty via Rapid Endochondral Ossification.* Stem Cell Reviews and Reports: p. 10.1007/s12015-023-10554-w..

[72] Ayturk, U.M., et al., Single-cell RNA sequencing of calvarial and long-bone endocortical cel ls. J. Bone Miner. Res. : Off. J. Am. Soc. Bone Mineral Res.. 35(10): p. 1981-1991..

[73] Jeyachandran, D., et al., *A Bioglass-Poly(lactic-Co-Glycolic Acid) Scaffold@Fibrin Hydrogel Cons truct to Support Endochondral Bone Formation.* Advanced Healthcare Materials: p. e2300211..

[74] Aprile, P. and D.J. Kelly, Hydrostatic pressure regulates the volume, aggregation and chondrogeni c differentiation of bone marrow derived stromal cells. Front. Bioeng. Biotechnol. 8..

[75] Grogan, S.P., et al., Visual histological grading system for the evaluation of <i>in Vitro</i>–generated neocartilage. Tissue Eng.. 12(8): p. 2141-2149..